Empowering Multicomponent Cathode Materials for Sodium Ion Batteries by Exploring Three-Dimensional Compositional Heterogeneities

Journal:	*Energy & Environmental Science*
Manuscript ID	EE-ART-01-2018-000309.R1
Article Type:	Paper
Date Submitted by the Author:	25-Apr-2018

Complete List of Authors:	Rahman, Muhammad; Virginia Polytechnic Institute and State University, CHEMISTRY Xu, Yahong; SLAC National Accelerator Laboratory Cheng, Hao; Xiamen University Shi, Qianli; Virginia Polytechnic Institute and State University Kou, Ronghui; Argonne National Laboratory Mu, Linqin; Virginia Polytechnic Institute and State University, CHEMISTRY Liu, Qi; Argonne National Laboratory Xia, Sihao; SLAC National Accelerator Laboratory Xiao, Xianghui; Argonne National Laboratory Sun, Chengjun; Argonne National Laboratory, Advanced Photon Source Sokaras, Dimosthenis; SLAC National Accelerator Laboratory, Stanford Synchrotron Radiation Lightsource Nordlund, Dennis; Stanford Synchrotron Radiation Lightsource, Zheng, Jin-Cheng; Xiamen University Liu, Yijin; Stanford Synchrotron Radiation Lightsource, Lin, Feng; Lawrence Berkeley National Laboratory, Environmental Energy Techonologies Division

Empowering Multicomponent Cathode Materials for Sodium Ion Batteries by Exploring Three-Dimensional Compositional Heterogeneities

Muhammad Mominur Rahman,[a] Yahong Xu,[b] Hao Cheng,[c] Qianli Shi,[a] Ronghui Kou,[d] Linqin Mu,[a] Qi Liu,[e] Sihao Xia,[b] Xianghui Xiao,[d] Cheng-Jun Sun,[d] Dimosthenis Sokaras,[b] Dennis Nordlund,[b] Jin-Cheng Zheng,[c] Yijin Liu,[b*] Feng Lin[a*]

a) Department of Chemistry, Virginia Tech, Blacksburg, VA, 24061, USA
b) Stanford Synchrotron Radiation Lightsource, SLAC National Accelerator Laboratory, Menlo Park, California 94025, USA
c) Department of Physics and the Collaborative Innovation Center for Optoelectronic Semiconductors and Efficient Devices, Xiamen University, Xiamen 361005, China; Xiamen University, Malaysia, 439000, Sepang, Selangor, Malaysia
d) Advanced Photon Source, Argonne National Laboratory, Argonne, Illinois 60439, USA
e) Department of Physics, City University of Hong Kong, Kowloon, Hong Kong

Corresponding authors: Y.L. liuyijin@slac.stanford.edu F.L. fenglin@vt.edu

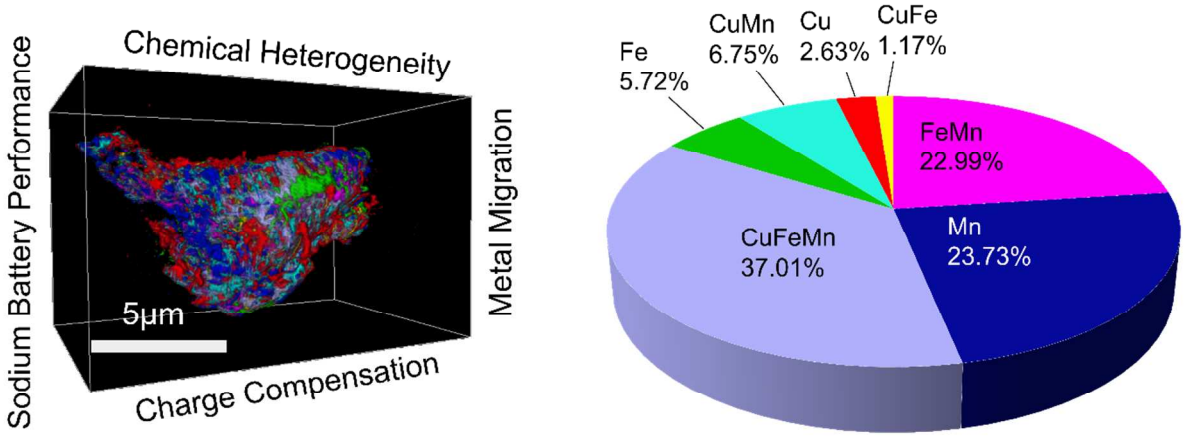

Three-dimensional compositional heterogeneities in sodium layered cathode materials were demonstrated to achieve good battery performance and exhibit depth-dependent charge compensation and metal migration.

Broader Context

Sodium ion batteries hold the potential to revolutionize the field of energy storage by enabling cheap and abundant layered transition metal oxide cathodes. However, high energy cathode materials must be designed to reduce the performance gap between sodium ion batteries and commercial lithium ion batteries. Multicomponent cathode materials with homogeneous distribution of transition metal ions has been the acclaimed way of synthesizing layered cathodes for alkali metal ion batteries. Instead of following the traditional route, this study focuses on developing three dimensional heterogeneous distribution of transition metal ions to promote high performance sodium layered cathodes. Three dimensional heterogeneity was manifested to improve the cycle life and specific capacity of $Na_{0.9}Cu_{0.2}Fe_{0.28}Mn_{0.52}O_2$. We investigated the chemical environment of the material as a function of depth and state of charge. We further investigated the pathway of capacity fading and found that Mn segregation to the surface of particles might account for the capacity fading upon prolonged cycling. Thus, our study provides insight into the effect of transition meal heterogeneity in the performance of cathode materials as well as enlightens a path towards further stabilizing Mn based layered oxide materials.

Abstract

Affordable sodium ion batteries hold great promise for revolutionizing stationary energy storage technologies. Sodium layered cathode materials are usually multicomponent transition metal (TM) oxides and each TM plays unique roles in operating cathode chemistry, e.g., redox activity, structural stabilization. Engineering the three-dimensional (3D) distribution of TM cations in individual cathode particles can take advantage of depth-dependent charging mechanism and enable a path towards tuning local TM–O chemical environments and building resilience against cathode–electrolyte interfacial reactions that are responsible for capacity fading, voltage decay and safety hazards. In this study, we create 3D compositional heterogeneity in a ternary and biphasic (O3-P3) sodium layered cathode material ($Na_{0.9}Cu_{0.2}Fe_{0.28}Mn_{0.52}O_2$). The cells containing this material deliver stable voltage profiles, discharge capacities of 125 mAh/g at C/10 with almost no capacity fading after 100 cycles and 75 mAh/g at 1C with negligible capacity fading after 200 cycles. The direct performance comparison shows that this material outperforms other materials with similar global compositions but different mesoscale chemical distributions. Synchrotron X-ray spectroscopy/imaging and density functional theory studies reveal depth-dependent chemical environments such as charge compensation and strength of orbital hybridization. Finally, 3D spectroscopic tomography enlightens the path towards optimizing multicomponent sodium layered cathode materials, that is to prevent the migration of TMs upon prolonged cycling. The study reports an inaugural effort of multifaceted and counterintuitive investigation of sodium layered cathode materials and strongly implies that there is plenty of room at the bottom by tuning nano/meso scale chemical distributions for stable cathode chemistry.

1. Introduction

Electrochemical energy storage technologies are revolutionizing the way that our society generates and consumes energy, particularly in the area of clean and renewable energy. The infinite variety of storage demands necessitate a range of battery chemistries that can target the specific performance criteria of each application. For example, grid energy storage and electric vehicles call for different battery solutions although they both require high energy/power density, low cost, long cycle life and excellent safety[1]. Grid energy storage would require much cheaper battery chemistries that are capable of levelling peak load and adjusting intermittency of renewable energy resources[2–4], whereas electric vehicles would require the ones that can deliver a good accelerating power and a long cruising distance[5]. Sodium ion batteries and lithium ion batteries are considered excellent batteries of choice for grid energy storage[4] and electric vehicles[6], respectively. The design of these batteries can follow the dual-intercalating rocking chair configuration, and importantly, layered oxides are considered one of the most promising cathode materials for both families of batteries[4,7,8]. In fact, the advancement of sodium and lithium layered cathodes have synergistically promoted each other, since the synergistic design of materials is possible due to their similar local coordination chemistry[4,7–10]. However, there are major differences between these two chemistries. More options of stoichiometry and transition metals (TMs) are available for sodium layered cathodes compared to those for the lithium counterparts[3,11–13], including flexibility in the type of intercalating ion[14]. Furthermore, sodium layered cathodes exhibit distinct voltage profiles, such as multiple voltage plateaus, due to the larger Na^+ ionic size and charge ordered configuration in sodium layered oxides[15–19] which result in suppressed specific capacity and low rate capability[20]. These unique characteristics of sodium layered cathodes open up enormous opportunities for studying the fundamental processes of alkali metal ions interacting with layered oxide materials as well as for improving sodium ion batteries for practical applications.

Universal to many battery chemistries, interfacial reactions between a layered oxide cathode and electrolytic solution impact cathode electrochemical properties thus influencing the overall performance of a battery. Typical interfacial reactions include but not limited to generation of cathode–electrolyte interphases (CEIs)[21,22], electrolyte decomposition[23–25], and surface reconstruction of cathode particles[26,27]. These reactions, along with other factors such as

crack formation[28,29] and dissolution of transition metal cations[30,31], impede the effort to increase the energy/power density and cycle life of alkali metal ion batteries. Numerous methods have been proposed to tackle these challenges, including surface coating[32,33], elemental substitution[34,35] and three-dimensional (3D) compositional control[36,37]. In particular, we have witnessed a number of successful examples towards engineering the surface of cathode particles (e.g., coating, metal segregation) for lithium ion batteries[32,34–36,38]. However, the parallel effort in sodium counterparts has been rather limited. To make further progress in sodium ion batteries, sodium layered cathode materials must be stabilized against undesired interfacial reactions. A recent study by Meng and coworkers showed that a thin layer of Al_2O_3 coating on layered P2-$Na_{2/3}Ni_{1/3}Mn_{2/3}O_2$ could effectively improve Coulombic efficiency and decrease cell impedance[39]. Most recently, our group applied a facile "cocktail" method to create conformal artificial CEI layers on O3-$NaNi_{1/3}Fe_{1/3}Mn_{1/3}O_2$ materials, which improved cycle life, shelf life and voltage stability[40]. TM*nd* orbitals undergo dynamic evolution upon electrochemical charging and discharging, which then influences the O*2p* occupancy through the TM*nd*–O*2p* orbital hybridization and alters the surface reactivity of cathode particles towards electrolytic solution. These processes contribute to the well-known problems of metal dissolution[31] and surface reconstruction[27] in alkali metal ion cathode materials. A layered oxide cathode material usually consists of multiple types of TMs, and the *d* orbitals of each TM have different degrees of hybridization with the local O*2p* orbitals. Therefore, an alternative approach for stabilizing interphases is to modify TM distribution at surfaces thus minimizing the participation of oxygen anions in the charge compensation. Such an approach has been found successful in lithium layered cathodes such as $LiNi_xMn_yCo_zO_2$ materials, for example, gradient distribution of cations[41] and selective metal segregation[37]. We conjecture that an equivalent approach for sodium layered cathode materials can potentially generate new insights into developing high-energy and long-life sodium ion batteries.

In this study, we adopted a simple approach to synthesize $Na_{0.9}Cu_{0.2}Fe_{0.28}Mn_{0.52}O_2$ materials with a heterogeneous 3D metal distribution, characterized by 3D full-field transmission X-ray microscopy (TXM). The best battery performance was achieved for the $Na_{0.9}Cu_{0.2}Fe_{0.28}Mn_{0.52}O_2$ material synthesized from the precursor with Cu-enriched surface (i.e., CFM-Cu). The cells containing this material delivered practical discharge capacities of 125 mAh/g at C/10 with zero capacity fading after 100 cycles and 75 mAh/g at 1C with only

negligible capacity fading after 200 cycles. These materials exhibited depth-dependent charge compensation that was not reported in the literature[39,42,43]. We also probed the degradation mechanism of these materials and discovered that inhibiting metal migration is critical for achieving stable cathodes. We anticipate that the present study can enlighten the path towards designing compositional heterogeneities for high-energy and long-life sodium ion batteries.

2. Experimental Methods

2.1. Material synthesis

Precursors of $Na_{0.9}Cu_{0.2}Fe_{0.28}Mn_{0.52}O_2$ were synthesized by a co-precipitation method in four different procedures using salt solutions of $CuSO_4•5H_2O$ (Sigma Aldrich, 98%), $MnSO_4•H_2O$ (Sigma Aldrich, 99%) and $FeSO_4•7H_2O$ (Sigma Aldrich, 99%) and NaOH as a base solution. In the first procedure, all three transition metals were precipitated simultaneously to form a mixed hydroxide, and the resulting sample is referred as CFM-H. For other procedures, two transition metals were first precipitated together (Cu-Mn, Fe-Mn or Cu-Fe) followed by the precipitation of the third transition metal (Fe, Cu or Mn, respectively), thus coating the third metal on the mixed hydroxide of the other two. The material with Fe-Mn precipitation followed by Cu precipitation is referred as CFM-Cu, Cu-Mn precipitation followed by Fe precipitation as CFM-Fe, Cu-Fe precipitation followed by Mn precipitation as CFM-Mn. The salt and base solution concentrations were kept consistent for every synthesis variation. 0.097M $CuSO_4$ solution, 0.136M $FeSO_4$ solution and 0.253M $MnSO_4$ solutions in 150 mL water were used for all the syntheses. Taking the precursor synthesis of CFM-Cu as an example, a salt solution with $FeSO_4$ and $MnSO_4$ in water was prepared and kept under nitrogen protection. A 0.5M aqueous solution of NaOH with $NH_3•H_2O$ (molar ratio of NaOH/$NH_3•H_2O$ was 1.2/1) in 150 mL water was prepared and also kept under nitrogen protection. This must be noted that $NH_3•H_2O$ was utilized only in the synthesis of CFM-Cu to better control the pH value. $NH_3•H_2O$ was however not used in any other syntheses because of the tendency of Cu to complex with NH_3 when Mn is in solution. The complexing problem can be avoided in CFM-Cu because during Cu precipitation no Mn is present in the solution. For all other syntheses, the presence of Mn in solution causes Cu to complex with NH_3 and thus lowers the yield of precipitate with significant deviation from the intended composition. The salt solution of Fe and Mn and the base solution were simultaneously pumped into the starting solution (80 mL aqueous solution of NaOH and

$NH_3•H_2O$ with the molar ratio of $NaOH/NH_3•H_2O$=1.2/1 and pH value was adjusted to 10.5 by H_2SO_4) at a drop rate of ~2 mL/min with continuously stirring at 700-800 rpm and heating at 50 °C. The drop rate of the base solution was frequently tuned to allow the reaction to take place at pH 10.5±0.2, until the pH stabilized. After the precipitation of Fe and Mn was complete, Cu was subsequently precipitated onto the mixed hydroxide of Fe and Mn at the same stirring rate, temperature and pH value. The final precipitate was then collected, washed and filtrated with DI water and dried in vacuum oven overnight at 100 ºC. The dried precursor was then mixed with nanosized Na_2CO_3, first by gently mixing the precursor and Na_2CO_3 using mortar and pestle and then by mixing in a speed mixer at 1500 rpm for ample amount of time to ensure thorough mixing. The mixed precursor with Na_2CO_3 was then calcined in a box furnace at 850 ºC for 10 hours to obtain the final CFM-Cu $Na_{0.9}Cu_{0.2}Fe_{0.28}Mn_{0.52}O_2$ powder.

Chemical desodiation was performed on CFM-Cu to mimic the deintercalation of Na^+ from the lattice through the electrochemical method. NO_2BF_4 in acetonitrile was used as the oxidant solution for chemical desodiation. Two solutions of oxidant NO_2BF_4 were prepared with the oxidant being equal to 50 mole% and 75 mole% of $Na_{0.9}Cu_{0.2}Fe_{0.28}Mn_{0.52}O_2$. CFM-Cu was then dispersed in the oxidant solutions and stirred in an Ar-filled glovebox for 24 hours at room temperature. The desodiated samples were then transferred out of the glovebox, centrifuged, dried overnight in a vacuum oven and then pressed into pellets for X-ray Raman spectroscopy measurements.

2.2.Materials Characterization

The morphology of the materials was evaluated by scanning electron microscopy (FEI Quanta 600 FEG) operated with an accelerating voltage of 5 kV. The instrument is equipped with a Bruker EDX and capable of taking images in both back-scattered and secondary electron modes. The global elemental composition of all four materials was evaluated through ICP-AES analysis. The ICP instrument is a Spectro ARCOS SOP (side-on or radial view of the Plasma interface) made by Spectro Analytical Instruments, Inc. The instrument has a relative standard deviation within 2% higher than background equivalent concentration for multiple sequential elemental analysis. The powder XRD patterns of the **Figures 1** and **S1** were acquired on a PANalytical X-ray diffractometer with the Cu K_α (λ=1.5406 Å) radiation. Soft X-ray absorption spectroscopy (XAS) measurements were performed on the 31-pole wiggler beamline 10-1 at

Stanford Synchrotron Radiation Lightsource (SSRL) using a ring current of 350 mA and a 1000 l·mm spherical grating monochromator with 20 μm entrance and exit slits, providing ~10^{11} ph·s^{-1} at 0.2 eV resolution in a 1 mm^2 beam spot. Data were acquired under ultrahigh vacuum (10^{-9} Torr) in a single load at room temperature using total electron yield (TEY), where the sample drain current was collected. All spectra were normalized by the current from freshly evaporated gold on a fine grid positioned upstream of the main chamber. XAS samples were mounted on an aluminum sample holder with double-sided carbon tape in an Ar-filled glovebox, and transferred to the load-lock chamber in a double-contained container, using a glove bag purged with argon for the transfer. Hard XAS measurements (Cu and Mn K-edge XAS) were performed in transmission mode using a Si (220) monochromator at the SSRL Beamline 4-1. The absorption energy was calibrated by using the first inflection points in the spectra of Mn metal foil reference at 6539 eV for Mn K-edge and Cu metal foil reference at 8979 eV for Cu K-edge. The hard XAS Fe K-edge spectra were carried out in transmission mode at Beamline 20-BM-B of the Advanced Photon Source. The incident beam was monochromatized by using a Si(111) fixed-exit, double-crystal monochromator. The full-field transmission X-ray microscope (TXM)[44] on Beam Line 6-2c at SSRL was used to perform 3D tomography and spectroscopic imaging analysis of heterogeneous CFM-Cu. The energy range on the instrument is ~4.5 to 13 keV, capable of spectroscopic imaging of transition metals in cathode materials and also of absorption contrast imaging of other materials. 3D elemental mapping was accomplished via acquisition of tomography above and below the X-ray absorption edge of the transition metals[45,46]. The segmentation of the 3D elemental maps is performed based on the quantitative analysis of the histogram of the 3D data (**Figure S13**). The elemental maps were first binarized before the elemental associations were evaluated. An in-house developed software package known as TXM-Wizard was used for the analysis of all the TXM data[47]. X-ray Raman Spectroscopy on Beam Line 6-2b at SSRL was used to obtain O K-edge spectra of chemically desodiated CFM-Cu samples. The incident beam was monochromatized with two monochromators including Si(111) and Si(311) as well as collimating and focusing optics.

2.3.Electrochemical Characterization

Composite cathodes were prepared by thoroughly mixing a slurry of active powder (80 wt%), carbon black (15 wt%), polyvinylidene fluoride (PVDF, 5%) and 1-methyl pyrrolidone (NMP)

solvent and casting the slurry onto carbon-coated aluminum foils. The coated aluminum foils were then dried in a vacuum oven at 120 °C overnight and stored in an argon-filled glovebox (H_2O<0.5 ppm, O_2<0.5 ppm). Hard carbon material was supplied by an independent supplier. A slurry was prepared with 90% hard carbon, 5% PVDF binder and 5% carbon black and casted into a carbon coated aluminum foil. The coated foil was then dried in vacuum oven overnight at 120°C. The pre-sodiation of the hard carbon anode was performed using Na metal anode at 100 μAh rate for 60 hours. CR2032 coin cells were assembled using Whatman glass fibers as the separator, pure Na foil (Alfa Aesar) as the anode and a saturated solution (~ 0.56M) of $NaPF_6$ in propylene carbonate (PC) as the electrolytic solution. The full cell with bare hard carbon used 1:1 weight ratio of EC DEC and 1M $NaClO_4$ as the salt. The pre-sodiated hard carbon still used saturated solution of $NaPF_6$ (0.56M) with PC as the electrolyte. The performance of coin cells was measured using a Wuhan Land Battery Testing System at room temperature. The charge and discharge rate were set based on 100 mAh/g as the base capacity (1C current density is 100 mA/g-active material). All the electrochemical data including specific capacity and middle voltage were processed through the LANDdt software. Middle voltage is defined at the voltage where half of the discharge capacity is obtained. The middle voltage analysis enables monitoring the growing cell impedance due to side reactions during electrochemical cycling. The electrodes were removed from coin cells, rinsed with dimethyl carbonate and dried in an argon-filled glovebox for synchrotron X-ray studies. The electrodes were sealed under argon and then transferred to the synchrotron beamlines using a homemade system to prevent exposure to air and moisture.

2.4.Computational details

We have performed first-principles plane-wave pseudopotential calculations based on density-functional theory (DFT), as implemented in Quantum Espresso simulation package[48], for Na-ion battery materials. The calculations made use of the spin-dependent generalized gradient approximation of Perdew, Burke, and Ernzerhof (PBE)[49], including Hubbard-U corrections following the formalism developed by Dudarev *et al.*[50]. The ultra-soft pseudopotential[51] with energy cutoff of 650 eV and 2x2x1 supercell with a 6x6x2 Γ-centered k-point mesh for Brillouin zone were used in our calculation. The atomic ratio Cu:Fe:Mn=3:4:5 (corresponding to $Na_{1-x}Cu_{0.25}Fe_{0.33}Mn_{0.42}O_2$) was used for modeling crystal structure of sodium layered cathode material

and a large number of cation arrangements have been considered by using the enumeration method by Hart et al[52,53]. The unit cell and atomic positions of all structures in the Na-ion battery materials were optimized until the atomic forces were less than 0.025eV/Å. Because the sodium layered cathode material studied in this work shows significant heterogeneity, it is difficult to model heterogeneity with a moderate size of supercell. The chosen size of 2x2x1 supercell with certain atom ratio (although slightly different from nominal composition of samples) is more likely to show the electronic properties of supercell with homogeneity in long-range scale (e.g., supercell is repeating in large scale), but at the same time with short-range local feature of heterogeneity within the supercell (namely, non-equilibrium sites for transition metals).

The optimized crystal structure is presented in **Figure S14a** and corresponding desodiation phases have been determined by ranking their total energy at each composition. We perform the charge-transfer analysis for the desodiation process (**Figure S14a-c**), the effective charge on atoms for each state are obtained by Bader method[54]. The relative transfer charge for transition metal in $Na_{1-x}Cu_{0.25}Fe_{0.33}Mn_{0.42}O_2$ is calculated as

$$\Delta e_s = \overline{e_{s,x}} - \overline{e_{s,x=0}}$$

where $\overline{e_{s,x}}$ is the average charge of transition metal s with composition x. The obtained transfer charges for each transitional metal averaged within supercell are shown in **Figure S14c**. While for local charge distribution of transition metals at different sites in the supercell, they are shown in **Figure S15**.

3. Result and Discussion

3.1. Physicochemical Characterization of Pristine Materials

Instead of synthesizing layered transition metal oxides as one single solid solution, adopting a synthesis method that introduces heterogeneity in the distribution of transition metals may provide a new avenue for tuning the electrochemical performance of layered oxide cathodes for alkali ion batteries[41,55]. CFM-Cu was chosen to study how the heterogeneity plays roles in the electrochemistry and interfacial phenomena of transition metal oxide cathodes.

ICP-AES analysis revealed that the global chemical compositions of all four materials (CFM-Cu, CFM-Mn, CFM-Fe and CFM-H) are close to the nominal composition (Cu: Fe: Mn = 0.2:0.28:0.52) **(Table S1)**.

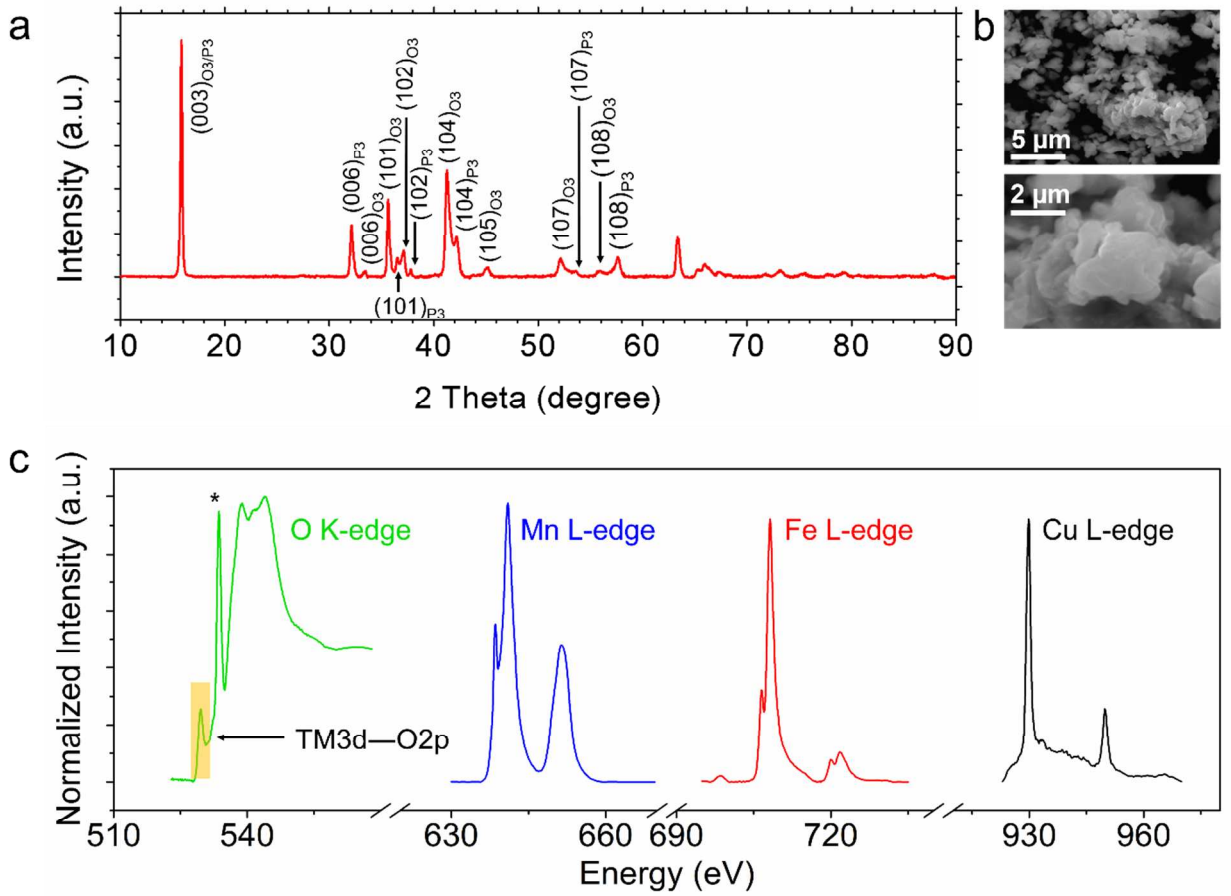

Figure 1. Physicochemical characterization of the pristine CFM-Cu powder. (a) XRD pattern of the pristine CFM-Cu powder. (b) SEM micrographs of the pristine CFM-Cu powder. (c) Soft XAS spectra (TEY mode) of the pristine CFM-Cu powder, where the peak labeled with "*" originated from the surface carbonate species.

The heterogeneous nature of these materials was evident from the XRD patterns. The XRD pattern of CFM-Cu revealed that it was not a single phase material, rather a mixture of an O3 phase and a P3 phase (**Figure 1**). Similar type of XRD pattern was also observed for CFM-Fe and CFM-H whereas CFM-Mn is mostly O3 phase **(Figure S1)**. The Rietveld refinement was not performed due to the fact that any lattice model would fail to account for the heterogeneous

nature of these materials (**Figures 2 and 3** discussed later). Nevertheless, the peaks were assigned to different crystallographic planes based on previous reports[43,56].

The agglomeration of the submicron-sized CFM-Cu primary particles did not result in secondary particles of well-defined morphology. The secondary particles were mostly random shaped **(Figure 1b).** In contrast, other three materials differed greatly in morphology from CFM-Cu **(Figures S2, S3** and **S4)**. CFM-Fe, CFM-Mn and CFM-H all had nearly spherical secondary particles. The drastically different morphology of CFM-Cu compared to other three materials can be attributed to the synthesis method of the precursors. Precursor synthesis of CFM-Cu was aided by NH_4OH, whereas for all other syntheses, NH_4OH was eliminated to avoid complexing of Cu with NH_3 that can significantly lower the yield of the product. As discussed in the Experimental Method, CFM-Cu was the only synthesis variation that could avoid the complexing of Cu. The absence of NH_4OH might have aided the formation of spherical particles in CFM-Fe, CFM-Mn and CFM-H.

Soft XAS was performed to understand the oxidation states of transition metals and surface oxygen speciation in the pristine CFM-Cu powder (**Figure 1c**). Soft XAS in the TEY mode probes mostly the surface region of particles, with 5-10 nm depth sensitivity[57]. The spectra revealed that the material is predominantly populated with Cu^{2+}, Fe^{3+} and Mn^{4+} at the surface. The region of interest in the O K-edge XAS is the pre-edge region in the range of 530-540 eV because it provides information about the TM3d–O2p hybridization and carbonyl groups. The O K-edge peak marked with an "*" is attributed to the transition to π^*(C=O) in the carbonate group. The carbonate could have originated either from unreacted sodium carbonate or reaction of lattice Na^+ with atmospheric CO_2 and moisture. We also observed a clear sign of TM3d–2Op hybridization in the O K-edge XAS spectrum. The deconvolution of Mn3d–O2p, Fe3d–O2p and Cu3d–O2p hybridization states was not attempted because of the complex arrangement of the transition metals in the crystal lattice which was compounded by the heterogeneous nature of the material. After the material was processed into an electrode (the corresponding XAS spectra are shown in **Figure S5**), Mn^{4+} was somewhat reduced, which was likely associated with the redox reaction between NMP and cathode particles during the electrode formulation. The relative intensity of the carbonate π^*(C=O) compared with that of TM3d-O2p hybridization decreased

after the electrode formulation, indicating that the electrode formulation could effectively leach away some surface carbonate species[58].

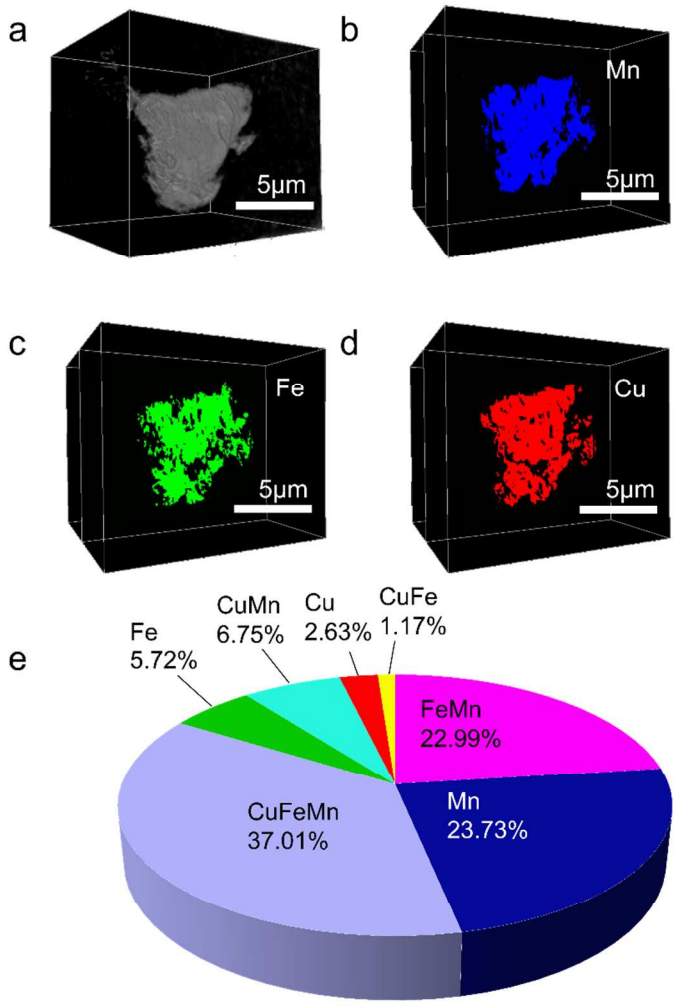

Figure 2. Transmission X ray tomography of CFM-Cu to analyze the mesoscale 3D elemental distribution and association. (a-d) 3D elemental distribution of CFM-Cu particles after calcination. The 3D structure of the particle was visualized by (a) single energy tomography. The multi energy tomography data with elemental sensitivity are visualized in (b-d) using virtual slice through the center of the particles, with blue, green and red representing (b) Mn, (c) Fe and (d) Cu, respectively. (e) The relative concentrations of the 3D elemental association calculated by using absorption correlation tomography.

We then quantified the 3D compositional heterogeneity for the pristine CFM-Cu powder using transmission X-ray microscopy (TXM) **(Figure 2).** The representative slices through the 3D volume of the secondary particle are shown in **Figures 2b-d**. All of the TMs were present at the individual secondary particle level, but their distributions were not identical. Subsequently, we quantified elemental associations for individual voxels throughout the secondary particle by performing a correlation analysis of the absorption coefficient as a function of the X-ray energies (above and below the K-edges of all the three transition metal elements, see Experimental Methods). As shown in **Figure 2e**, the material contains significant single metal association with Mn only association being the highest (23.73%). The Mn-Fe-Cu association was only 37.01% for the pristine CFM-Cu powder. More than 30% of the total voxels contain single transition metal (Cu only, Fe only and Cu only). Furthermore, we constructed elemental association maps to directly visualize the compositional heterogeneity in 3D (**Figure 3**). A large number of nanodomains deviated from the global CFM-Cu stoichiometry (Cu: Fe: Mn=0.2:0.28:0.52). While the bulk of secondary particles contains mostly Cu-Fe-Mn ternary phases, the surface contains phases of both single metal and binary metal associations (**Figure 3b**). Therefore, one can conclude that we have obtained a highly heterogeneous chemical distribution for the CFM-Cu material, which forms a chemical basis for studying the impact of compositional heterogeneity on battery performance. However, the elemental associations of various nanodomains can be further tuned through thermal annealing[59], pH and composition control, which opens up plenty of room for new research opportunities in the field of compositionally heterogeneous layered oxide materials.

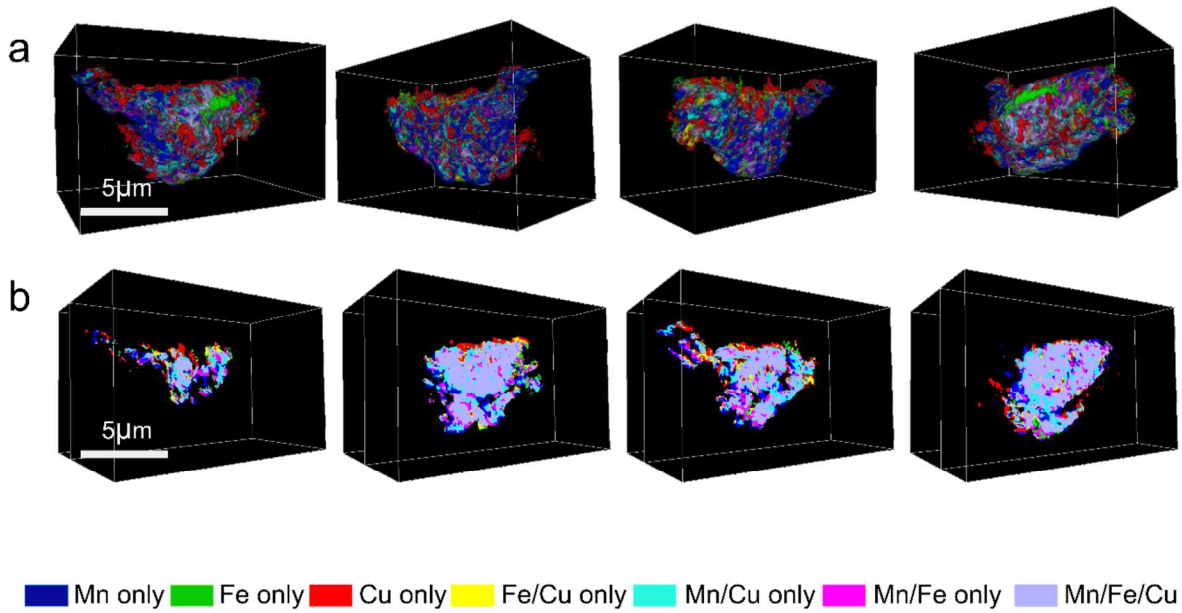

Figure 3. 3D elemental association maps of the pristine CFM-Cu powder generated using transmission X ray tomography. (a) 3D visualization of the elemental associations from different angles showing that the surface is dominated by single metal and binary metal associations, and (b) 2D elemental association maps cut through the particle at different depths to show the different elemental associations between the bulk and the surface. The bottom bars show the color codes for different elemental associations.

3.2. Electrochemical Performance Evaluation

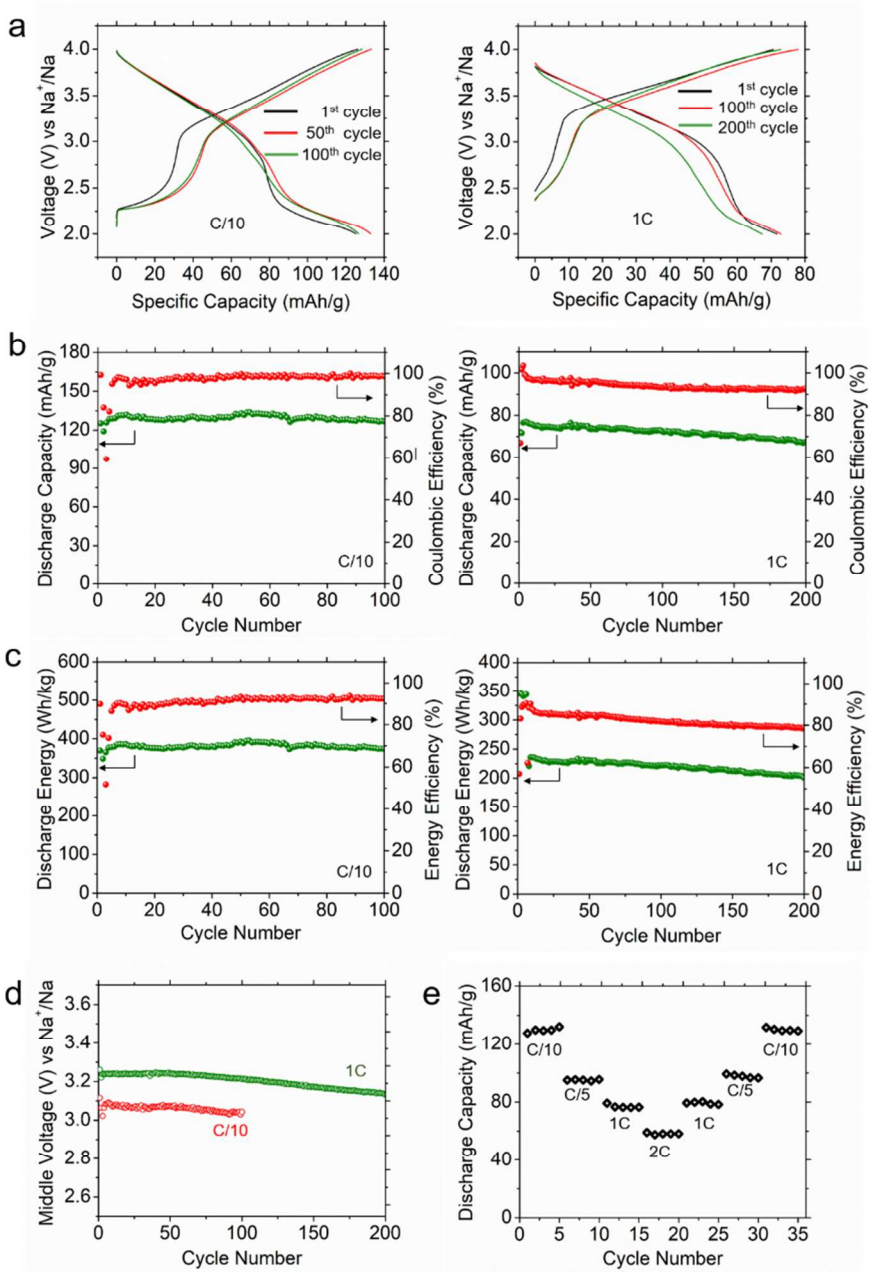

Figure 4. Electrochemical performance evaluation of CFM-Cu in Na half-cells. (a) charge/discharge curves at various cycles of CFM-Cu at (left) C/10 and (right) 1C rates in the voltage window of 2-4V vs Na^+/Na. (b) specific discharge capacities and Coulombic efficiencies of Na half-cell containing CFM-Cu at (left) C/10 and (right) 1C rates, (c) discharge energy and energy efficiency of CFM-Cu at (left) C/10 and (right) 1C rates, (d) middle voltage profiles of CFM-Cu vs Na^+/Na at C/10 and 1C rates for CFM-Cu, and (e) rate capability of CFM-Cu at different C rates, where symmetric charging and discharging rates were applied.

We studied the electrochemical performance of CFM-Cu to provide evidence that compositional heterogeneity can potentially offer a choice of designing cathode materials with good electrochemical performance. The cells containing CFM-Cu delivered initial specific discharge capacities of 125 mAh/g at C/10 and 75 mAh/g at 1C in the voltage range of 2-4V vs Na^+/Na (**Figure 4a**). These specific capacities are superior or comparable to those reported for materials with similar transition metal system[43,60,61]. The cells with CFM-Cu also delivered stable cycling with almost zero capacity fading after 100 cycles at C/10 and only negligible capacity fading after 200 cycles at 1C **(Figure 4b)**. It is rarely reported for a material which does not undergo any significant capacity fading after so many cycles at a slow charging/discharging rate such as C/10. Cells with CFM-Fe, CMF-Mn and CFM-H all had reasonably good electrochemical performance but were slightly inferior to that of CFM-Cu in terms of specific discharge capacity and cycle life (**Figures S7-S9**). CFM-Fe, CFM-Mn and CFM-H delivered initial specific discharge capacities of 89.7 mAh/g, 77.5 mAh/g and 91.7 mAh/g at C/10, respectively. In terms of cycle life at C/10, CFM-Fe, CFM-H and CFM-Mn showed capacity retentions of 83.2%, 88.9%, 94.6% after 100 cycles, respectively. At 1C rate, CFM-Fe, CFM-Mn and CFM-H showed capacity retentions of 79.7%, 81.5% and 89.3% after 200 cycles, respectively. To summarize, compared to other similar materials reported in the literature, not only did our best performing CFM-Cu delivered better or comparable cycle life and specific capacity but also the other three materials had comparable electrochemical performance[43,60,61].

Low first-cycle Coulombic efficiency is one of the characteristics of O3 type layered oxide cathodes[62]. However, the first-cycle Coulombic efficiency of CFM-Cu was impressively 99.3% at C/10. We hypothesize that the reason lies mostly in the biphasic nature of the material. CFM-Cu is a mixture of both O and P phases, where the first cycle Coulombic efficiency is low for O3 type materials but it is usually high for P type materials[63]. Thus we achieved synergetic effects in the biphasic CFM-Cu material for a high first-cycle Coulombic efficiency. This may help maintain sodium inventory in practical sodium ion batteries.

The cells containing CFM-Cu delivered a high discharge energy of 370 Wh/kg at C/10 and 220 Wh/kg at 1C **(Figure 4c)**. The initial discharge energy at C/10 provided by CFM-Fe, CFM-Mn and CFM-H were around 290 Wh/kg, 240 Wh/kg and 300 Wh/kg, respectively (**Figures S7b-S9b**). The specific energy delivered by these three materials at 1C was lowered to

around 180 Wh/kg, 175 Wh/kg and 190 Wh/kg, respectively (**Figure S7b-S9b**). The middle voltage profile for CFM-Cu was stable at approximately 3.1 V for C/10 and 3.25 V for 1C (**Figure 4d**). The reason for lower middle voltage at C/10 could be that at the slower charge/discharge rate (C/10), the capacity gain at the low voltage range (2.0-2.3 V) was significantly larger compared to that at 1C (compare voltage profiles in **Figure 4a**). Similar voltage plateau has previously been reported in the literature.[15,64]. However, we suspect that in this low voltage region (2.0-2.3V), kinetically driven processes play a dominant role. Slower charge/discharge rate like C/10 supports these processes. Hence, the capacity gain at the lower voltage at C/10 was significantly larger than that at 1C. Nevertheless, when the battery is discharged to lower than 2V at 1C, the low voltage plateau is further extended and the discharge capacity almost catches up with that of C/10 (**Figure S6**), thus further supporting our hypothesis.

Subsequently, we investigated the rate capability of the CFM-Cu material (**Figure 4e**), where we used identical charging and discharging rates at each given rate. At C/10, the initial specific discharge capacity was 127 mAh/g, whereas 76.2 mAh/g was delivered at 1C. The drop in the specific capacity between these two charging/discharging rates was 40%. Even though the drop was somewhat high, the capacity retention after full cycling at all C rates was impressive. Instead of losing capacity after full cycling, it increased slightly. The material delivered a specific capacity of 129 mAh/g at the very last cycle which indicates a capacity retention of 101.6%. This result illustrates the excellent rate capability of the material and implies that the material is capable of effectively handling different charging/discharging rates under practical conditions.

In order to provide further evidence of the practical applicability of CFM-Cu, we fabricated a full cell with the as prepared cathode material, using bare hard carbon and pre-sodiated hard carbon anodes. Pre-sodiation of hard carbon is usually done in order to account for the low first cycle Coulombic efficiency observed in bare hard carbon anodes[65–67]. The cycling performance of the material at 1C rate in terms of discharge capacity, discharge energy and middle voltage were evaluated for both full cells and is presented in **Figure S10**. Using the bare hard carbon, CFM-Cu in a full cell delivered 63 mAh/g initial capacity at 1C rate. The middle voltage and energy density derived from the material were about 3.1 V and 193 Wh/kg respectively. While the full cell with the pre-sodiated hard carbon delivered performance close to

that of a Na half-cell. The material in such a full cell could deliver a discharge capacity of 71mAh/g, a middle voltage of 3.2-3.3V and an energy density of 220 Wh/kg. This implies that with the advent of better anode materials, the potential of a cathode material in a full-cell can be completely realized. In summary, the heterogeneous CFM-Cu material can deliver reasonably high battery performance, implying that a homogeneous chemical distribution may not be crucial for achieving high performance cathode materials.

3.3. Depth Dependent Chemical Evolution

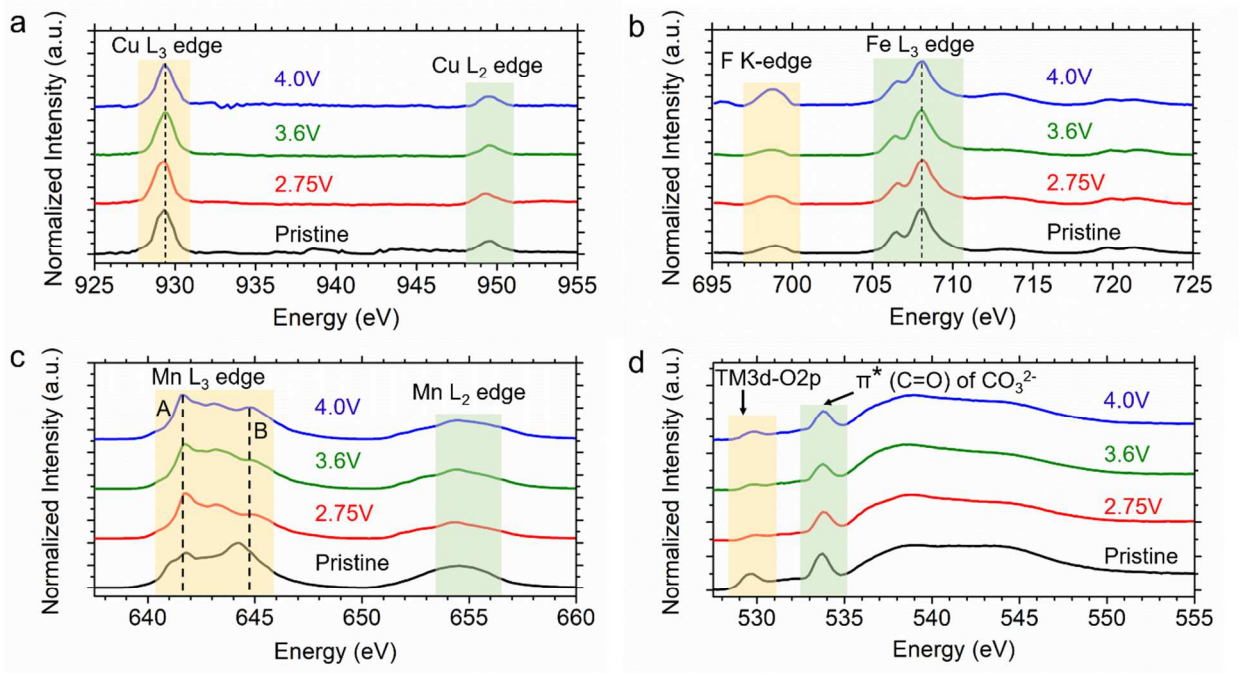

Figure 5. Surface sensitive soft XAS spectra (TEY mode) of CFM-Cu for (a) Cu L-edge, (b) Fe L-edge, (c) Mn L-edge, peaks labelled as A and B gradually changed in intensity as a function of charge and (d) O K-edge at different states of charge in the first charge cycle at C/10 rate. Color scheme: black spectra: pristine electrode, red spectra: charged to 2.75V, green spectra: charged to 3.6V and blue spectra: charged to 4.0V.

The surface of cathode particles has distinct chemical environments compared to the bulk, leading to drastically different charge compensation mechanism in alkali metal ion oxide cathode materials, i.e., depth-dependent charge compensation mechanism[57,68]. On the other hand, such mechanism also results in depth-dependent fading processes in cathode materials. For

example, the surface undergoes structural transformation[27] and the bulk undergoes extensive cation mixing[69]. Here we applied a combination of soft XAS, hard XAS, XRS and TXM to probe the depth-dependent charge compensation and fading mechanism for the heterogeneous CFM-Cu material at various states of charge and after prolonged cycling.

Surface sensitive soft XAS was used to investigate the evolution of TM oxidation states at different states of charge. At the top surface probed by the TEY mode, Cu remained relatively unchanged during charging and discharging processes (**Figure 5a and Figure S11a**), maintaining its +2 oxidation state[70]. Fe in the surface region was predominantly in Fe^{3+} oxidation state[71], during both charge and discharge **(Figure 5b and Figure S11b)**. Admittedly, we are aware that the differentiation of Fe^{3+} from Fe^{4+} using Fe L-edge soft XAS is challenging. The challenge is amplified by the fact that the Fe L-edge spectrum overlaps significantly with that of F K-edge[72]. The fluorine species originated from the electrolyte decomposition, PVDF binder or $NaPF_6$ residual. Mn was the most active among all the three transition metals at the surface. Mn was in the Mn^{4+} oxidation state[27] in the pristine powder (**Figure 1c**) and was slightly reduced after the CFM-Cu was processed into the electrode (**Figure S5**). During the early stage of the charging process, Mn underwent continuous reduction up to 2.75 V (compare the peak intensities in higher and lower energy side in **Figure 5c**). Upon the subsequent charging to 4 V, Mn was gradually oxidized, which can be seen by the increased intensity of the higher energy shoulder (B in **Figure 5c**) of the Mn L_3-edge. We conjecture that such a dynamic evolution of Mn oxidation states was attributable to the competing process between the Mn reduction by interfacial reaction and the Mn oxidation by the sodium deintercalation of Mn-rich nanodomains during the charging process. Subsequently, Mn underwent reduction upon discharging **(Figure S11c)**. As soft XAS in the TEY mode probed the surface region of the electrode, the observation suggested that the Mn redox process was irreversible at the surface, which is likely associated with the fading process of the cathode material (more discussion later). The pre-edge peak associated with the TM3d–O2p hybridization followed the similar trend as the Mn redox process (**Figure 5d**). This peak intensity decreased up to 2.75 V. Then the intensity of this peak experienced a gradual increase upon further charging to 4 V. The intensity of this peak decreased during the subsequent discharging **(Figure S11d**). While Fe and Cu experienced minimal changes at the surface, the concurrent evolution of TM3d–O2p hybridization and Mn oxidation state implies that Mn and O were strongly correlated and dominated the cathode–electrolyte interfacial reactions.

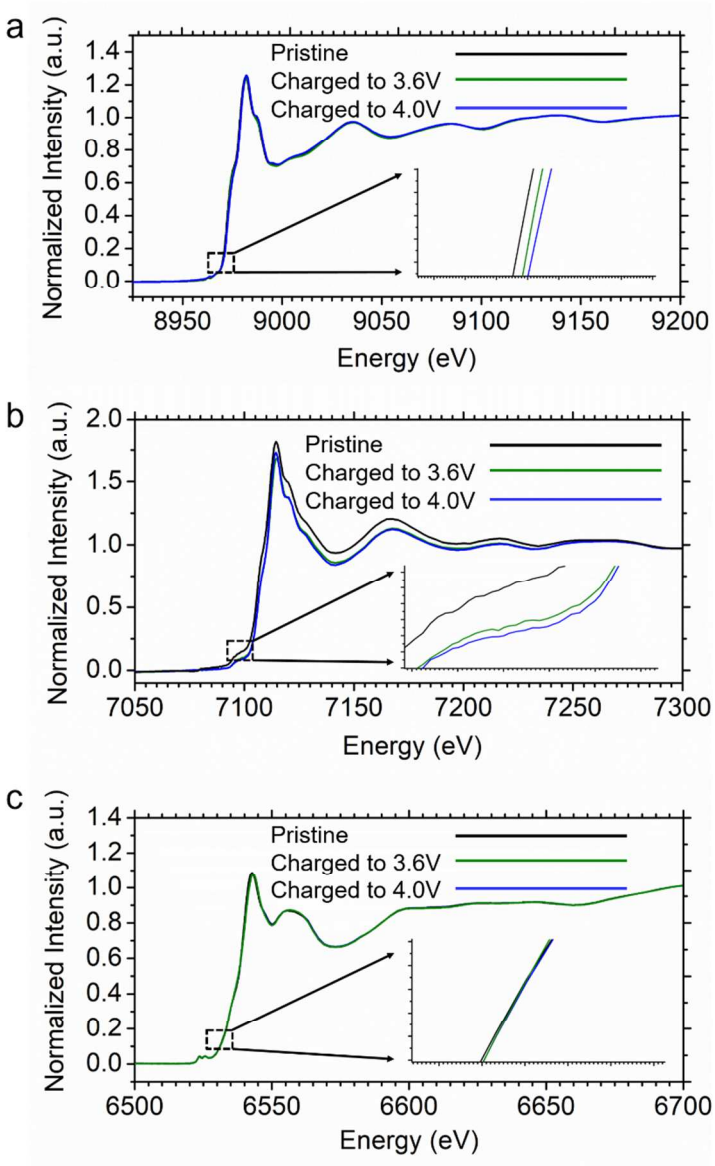

Figure 6. Hard XAS spectra of CFM-Cu for (a) Cu K-edge, (b) Fe K-edge and (c) Mn K-edge at different states of charge during the first charge cycle at C/10 rate. The inset shows the zoom-in of the boxed portion of the spectra.

Figure 6 shows the hard XAS spectra of the three transition metal elements at different states of charge during the first charging cycle at C/10 rate. Unlike what we have observed in the soft XAS, hard XAS revealed that Cu and Fe were electrochemically active in the bulk. The Cu K-edge spectrum shifted gradually to higher energy side revealing that Cu^{2+} was undergoing

oxidation (**Figure 6a**). On the way to discharge, the spectrum shifted to the lower energy side indicating reduction **(Figure S12a)**. Fe K-edge spectrum also showed a shift to the higher energy side during the charging process **(Figure 6b)** and a corresponding shift to the lower energy side during the discharge process **(Figure S12b)**. However, in case of Mn K-edge spectrum, no observable shift was monitored during either the charge **(Figure 6c)** or the discharge **(Figure S12c)**, thus reflecting the electrochemically inactive nature of Mn^{4+} in the bulk. It should be noted that Mn was redox active at the surface (**Figure 5c**), but the contribution from the surface was too trivial to create any observable change in the Mn K-edge XAS. In contrast, according to our DFT computational study, in a compositionally homogeneous material, all three transition metals are expected to exhibit redox activity (**Figure S14c**). Thus, the comparison reveals that compositional heterogeneity can influence the charge compensation mechanism of multicomponent materials.

Considering the fact that, in the theoretical model, the repeating unit is supercell, in long-range scale, it shows homogeneity, see for example, element-averaged charge transfers of Cu, Fe, and Mn with reduction of Na composition (**Figure S14c**). However, within a supercell, the sites for transition metals even with the same element are not equilibrium, it is highly possible to show short-range heterogeneity due to the localization of *d* orbitals and local feature of coordination with the changes of Na composition, as shown in differences of local charge transfer of transition metal (**Figure S15**) and the shift of band edge of transition metals in conduction band (**Figure S16, S17**). If the supercell is enlarged, the local feature of short-range heterogeneity will be more significant. Therefore, although our DFT calculations are utilizing a relative small supercell, it clearly shows the long-range homogeneity, but also shows local feature of short-range heterogeneity. For the case of remarkable heterogeneity of nanoparticles as shown in experiments, the significant electronic heterogeneity is thus expected. That may shed some light on the electronic origin of electrochemical performance of nanoparticles with high heterogeneity.

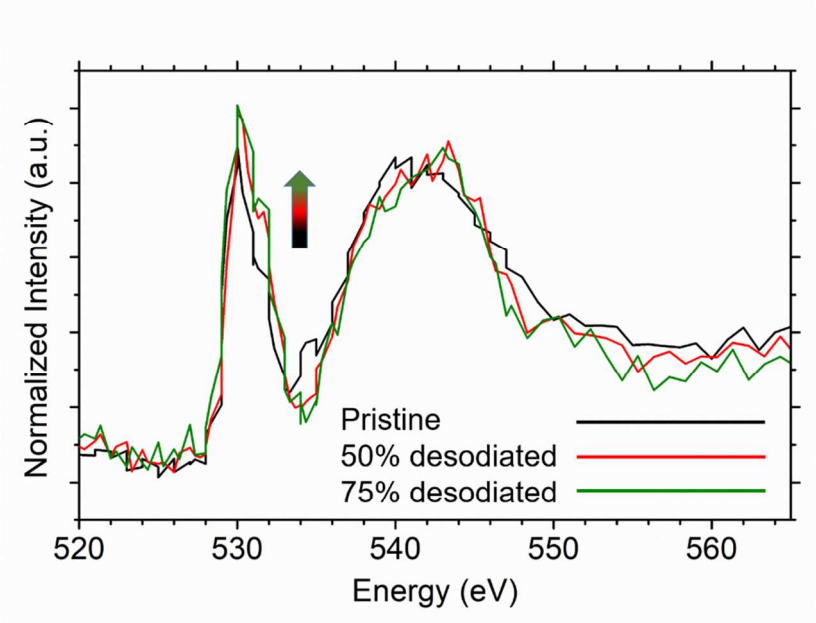

Figure 7. Oxygen K-edge X-ray Raman spectra of CFM-Cu at different chemically desodiated states; the arrow sign indicates the rising intensity of the TM3d–O2p peak with increasing desodiation level.

X-ray Raman spectroscopy (XRS) was performed on different chemically desodiated states of CFM-Cu to understand the chemical evolution of TM3d–O2p bond in the bulk of the particle during Na deintercalation. During chemical desodiation, the removal of sodium and change in oxidation states of the transition metals happen in a similar way as in electrochemical desodiation. **Figure 7** shows the O K-edge spectra of pristine, 50% desodiated and 75% desodiated CFM-Cu. The strength of TM3d-O2p hybridization was significantly more intense in the bulk (**Figure 7**) compared to the surface (**Figure 1c**) in the pristine powder, indicating different oxygen chemical environment from the surface to the bulk. The spectra clearly show a gradual change in the pre-edge peak intensity of O K-edge, indicating a dynamic electronic rearrangement in the TM3d–O2p hybridization in the bulk of the material upon sodium deintercalation. At higher desodiation level, the intensity of the TM3d–O2p peak increased. Soft XAS of CFM-Cu at different states of charge provided evidence of oxygen being active at the surface of the particles, dictating cathode-electrolyte interfacial reactions (**Figure 5d**). The XRS gave verification that oxygen was not only active at the surface but also in the bulk of the

particles of CFM-Cu. We believe that the oxygen activity in the bulk was attributed to the TM3d–O2p hybridization in the present case. In summary, the combination of soft XAS, hard XAS and XRS revealed the different chemical environments between the surface and the bulk of CFM-Cu particles. Cu and Fe in the bulk were responsible for charge compensation and discharge capacity whereas Mn dominated the surface processes. Meanwhile, the strength of hybridization of TM3d—O2p got stronger from the surface to the bulk.

3.4. Phase Segregation and Transition Metal Migration

Thus far, we have demonstrated that the heterogeneous nature of CFM-Cu resulted in good electrochemical performance and showed depth-dependent charge compensation mechanism. However, this material still inevitably suffered from capacity fading upon prolonged cycling (>400 cycles). TXM analysis was performed on the material after 400 cycles at 1C rate to elucidate the failure mechanism and to enlighten a pathway for further stabilizing CFM-Cu.

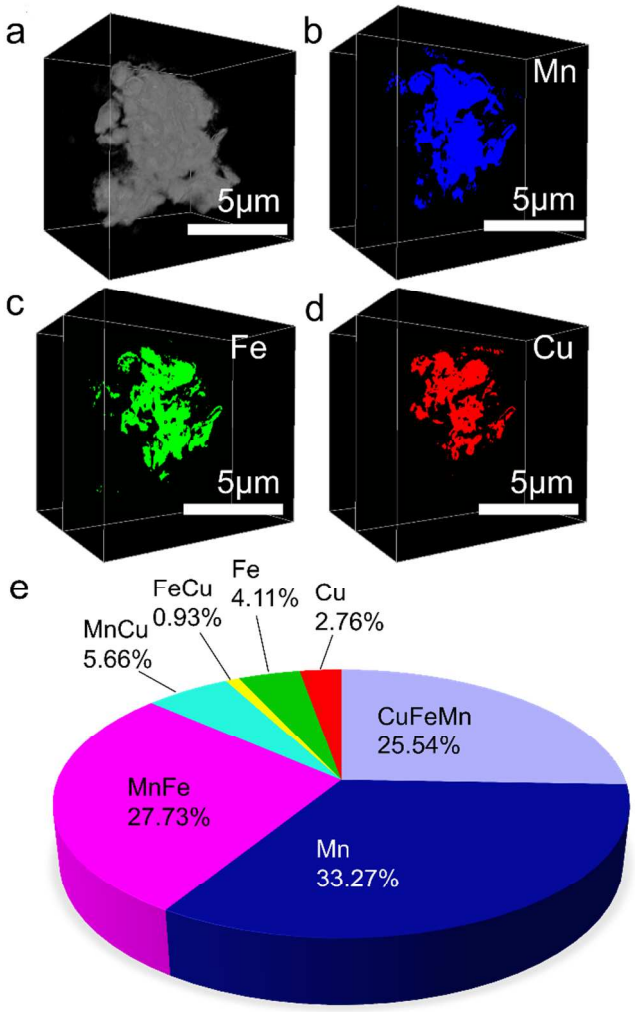

Figure 8. Transmission X-ray tomography of CFM-Cu to analyze change in elemental mapping and elemental association after 400 cycles at 1C rate. (a) 3D morphology of the CFM-Cu particle after cycling rendered from single energy tomography data. The visualization of elemental distribution in cycled CFM-Cu is conducted using multi energy tomography, with blue, red and green representing (b) Mn, (c) Fe and (d) Cu, respectively. (e) The relative concentrations of each elemental association in the cycled CFM-Cu particles as calculated by using absorption correlation tomography.

The transition metal association in various nanodomains differed significantly from those of pristine CFM-Cu powders. Most noticeably, the Cu-Fe-Mn association decreased and single metal association of Mn increased **(Figure 8e)**. Both two metal and single metal associations in

various nanodomains also differed to varying degree from those of the pristine powder (compare **Figure 8e** with **Figure 2e**). Furthermore, as evident from the 3D elemental distribution of the particles after cycling, both Cu and Fe had been mostly confined in the bulk of the particles while Mn stretched from the bulk to the surface (**Figure 8b**), indicating Mn migration to the surface of particles.

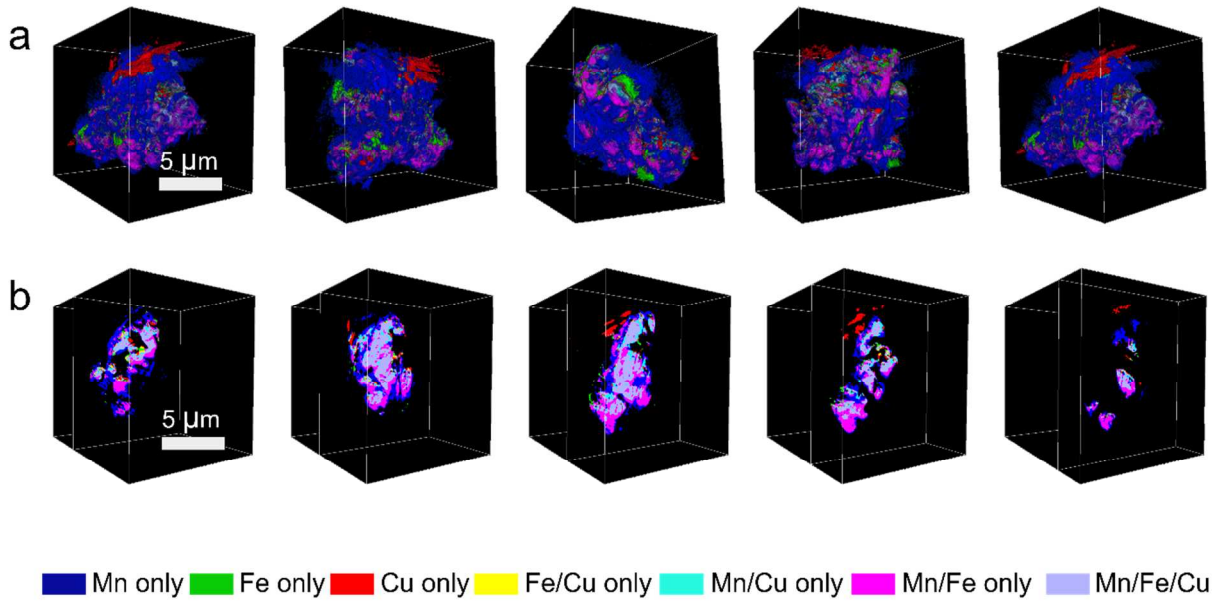

Figure 9. 3D elemental association maps of CFM-Cu generated using transmission X ray tomography after long term cycling (400 cycles at 1C rate) in a Na half-cell to visualize changes in elemental associations. (a) 3D resolved elemental associations at the surface of CFM-Cu after long term cycling, (b) 2D perception of the elemental associations in planes cut through the particle from the surface to the bulk at different depths. The bottom bars show the color codes for different elemental associations.

Figure 9 shows the 3D elemental association maps of CFM-Cu particles in various nanodomains after 400 cycles. This provides further evidence on Mn migration to the surface. Unlike pristine powder, **Figure 9a** shows that the surface of the particle was mostly populated with Mn only association (compare **Figure 3a** with **Figure 9a**). The subsequent decrease in three metal association (Cu-Fe-Mn) bring to light the probable phase segregation in the material.

Thus, the failure mechanism in CFM-Cu is likely related to Mn segregation from Cu-Fe-Mn association and its consequential deposition and reduction at the surface of cathode particles, which is consistent with the observation of soft XAS, hard XAS and XRS. Similar metal segregation was reported by some of our coauthors on lithium/manganese rich NMC materials[73]. Therefore, these results collectively provide compelling evidence that stabilizing the material against phase segregation and elemental migration on long term cycling could be a path towards more stable sodium layered cathode materials.

4. Conclusion

A homogeneous or defined distribution of transition metal cations has been considered the rule of thumb for developing high performance multicomponent cathode materials in alkali metal ion batteries. Counterintuitively, we reported a good performing sodium layered cathode material resulting from a highly heterogeneous 3D elemental distribution. The material investigated (CFM-Cu) had almost no capacity fading at C/10 after 100 cycles and only negligible capacity fading at 1C after 200 cycles. We thoroughly studied the dynamic chemical environments of the transition metals and oxygen anions as a function of depth upon charging and discharging, and discovered that the heterogeneity in transition metal distribution also led to depth-dependent charge compensation mechanism in the material. Depth-dependent charge compensation was evident from the disparity in redox activity of transition metals from the surface to the bulk. Mn mostly dictated the cathode-electrolyte interfacial reactions while Cu and Fe contributed to the overall charge compensation process of the material in the bulk. In addition, our combined experimental and theoretical studies also revealed that compositional heterogeneity can influence the charge compensation mechanism of multicomponent materials. Finally, we further evaluated the fading mechanism of the material and found that Mn segregation to the surface of particles was possibly responsible for capacity fading upon prolonged cycling. Therefore, our work not only demonstrated the effect of compositional heterogeneity on developing stable layered transition metal oxide cathodes but also provided a direction to further stabilize Mn-containing sodium layered cathode materials.

5. References

1 R. Van Noorden, *Nature*, 2014, **507**, 26–28.

2 V. Palomares, P. Serras, I. Villaluenga, K. B. Hueso, J. Carretero-González and T. Rojo, *Energy Environ. Sci.*, 2012, **5**, 5884–5901.

3 N. Yabuuchi, K. Kubota, M. Dahbi and S. Komaba, *Chem. Rev.*, 2014, **114**, 11636–11682.

4 H. Pan, Y.-S. Hu and L. Chen, *Energy Environ. Sci.*, 2013, **6**, 2338–2360.

5 D. Andre, S.-J. Kim, P. Lamp, S. F. Lux, F. Maglia, O. Paschos and B. Stiaszny, *J. Mater. Chem. A*, 2015, **3**, 6709–6732.

6 M. Armand and J.-M. Tarascon, *Nature*, 2008, **451**, 652–657.

7 W. Liu, P. Oh, X. Liu, M.-J. Lee, W. Cho, S. Chae, Y. Kim and J. Cho, *Angew. Chemie Int. Ed.*, 2015, **54**, 4440–4457.

8 M. D. Slater, D. Kim, E. Lee, M. M. Doeff and C. S. Johnson, *Adv. Funct. Mater.*, 2013, **23**, 947–958.

9 C. Delmas, C. Fouassier and P. Hagenmuller, *Phys. B+C*, 1980, **99**, 81–85.

10 M. M. Doeff, M. Y. Peng, Y. Ma and L. C. De Jonghe, *J. Electrochem. Soc.*, 1994, **141**, L145–L147.

11 M. S. Whittingham, *Chem. Rev.*, 2014, **114**, 11414–11443.

12 M. S. Whittingham, *Chem. Rev.*, 2004, **104**, 4271–4302.

13 H.-R. Yao, P.-F. Wang, Y. Wang, X. Yu, Y.-X. Yin and Y.-G. Guo, *Adv. Energy Mater.*, 2017, **7**, 1700189.

14 X. Wang, P. Hu, C. Niu, J. Meng, X. Xu, X. Wei, C. Tang, W. Luo, L. Zhou, Q. An and L. Mai, *Nano Energy*, 2017, **35**, 71–78.

15 X. Ma, H. Chen and G. Ceder, *J. Electrochem. Soc.*, 2011, **158**, A1307–A1312.

16 D. Buchholz, A. Moretti, R. Kloepsch, S. Nowak, V. Siozios, M. Winter and S. Passerini, *Chem. Mater.*, 2013, **25**, 142–148.

17 M. Sathiya, K. Hemalatha, K. Ramesha, J.-M. Tarascon and A. S. Prakash, *Chem. Mater.*, 2012, **24**, 1846–1853.

18 H. Yoshida, N. Yabuuchi and S. Komaba, *Electrochem. commun.*, 2013, **34**, 60–63.

19 R. Berthelot, D. Carlier and C. Delmas, *Nat. Mater. 2010 101*, 2011, **10**, 74–80.

20 W. Ren, M. Qin, Z. Zhu, M. Yan, Q. Li, L. Zhang, D. Liu and L. Mai, *Nano Lett.*, 2017, **17**, 4713–4718.

21 E. Peled and S. Menkin, *J. Electrochem. Soc.*, 2017, **164**, A1703–A1719.

22 H. Duncan, Y. Abu-Lebdeh and I. J. Davidson, *J. Electrochem. Soc.*, 2010, **157**, A528–A535.

23 A. Guéguen, D. Streich, M. He, M. Mendez, F. F. Chesneau, P. Novák and E. J. Berg, *J. Electrochem. Soc.*, 2016, **163**, A1095–A1100.

24 M. Gauthier, T. J. Carney, A. Grimaud, L. Giordano, N. Pour, H.-H. Chang, D. P. Fenning, S. F. Lux, O. Paschos, C. Bauer, F. Maglia, S. Lupart, P. Lamp and Y. Shao-Horn, *J. Phys. Chem. Lett.*, 2015, **6**, 4653–4672.

25 A. Jarry, S. Gottis, Y.-S. Yu, J. Roque-Rosell, C. Kim, J. Cabana, J. Kerr and R. Kostecki, *J. Am. Chem. Soc.*, 2015, **137**, 3533–3539.

26 S.-K. Jung, H. Gwon, J. Hong, K.-Y. Park, D.-H. Seo, H. Kim, J. Hyun, W. Yang and K. Kang, *Adv. Energy Mater.*, 2014, **4**, 1300787.

27 F. Lin, I. M. Markus, D. Nordlund, T.-C. Weng, M. D. Asta, H. L. Xin and M. M. Doeff, *Nat. Commun.*, , DOI:10.1038/ncomms4529.

28 P. Yan, J. Zheng, M. Gu, J. Xiao, J.-G. Zhang and C.-M. Wang, *Nat. Commun.*, 2017, **8**, 14101.

29 R. Xu, H. Sun, L. S. de Vasconcelos and K. Zhao, *J. Electrochem. Soc.*, 2017, **164**, A3333–A3341.

30 N. P. W. Pieczonka, Z. Liu, P. Lu, K. L. Olson, J. Moote, B. R. Powell and J.-H. Kim, *J. Phys. Chem. C*, 2013, **117**, 15947–15957.

31 J. A. Gilbert, I. A. Shkrob and D. P. Abraham, *J. Electrochem. Soc.*, 2017, **164**, A389–A399.

32 J. M. Zheng, J. Li, Z. R. Zhang, X. J. Guo and Y. Yang, *Solid State Ionics*, 2008, **179**, 1794–1799.

33 X. Wang and G. Yushin, *Energy Environ. Sci.*, 2015, **8**, 1889–1904.

34 H. Yu and H. Zhou, *J. Phys. Chem. Lett.*, 2013, **4**, 1268–1280.

35 S. Wolff-Goodrich, F. Lin, I. M. Markus, D. Nordlund, H. L. Xin, M. Asta and M. M. Doeff, *Phys. Chem. Chem. Phys.*, 2015, **17**, 21778–21781.

36 Y.-K. Sun, Z. Chen, H.-J. Noh, D.-J. Lee, H.-G. Jung, Y. Ren, S. Wang, C. S. Yoon, S.-T. Myung and K. Amine, *Nat. Mater.*, 2012, **11**, 942–947.

37 F. Lin, D. Nordlund, Y. Li, M. K. Quan, L. Cheng, T.-C. Weng, Y. Liu, H. L. Xin and M. M. Doeff, *Nat. Energy*, 2016, **1**, 15004.

38 Z. Chen, Y. Qin, K. Amine and Y.-K. Sun, *J. Mater. Chem.*, 2010, **20**, 7606–7612.

39 J. Xu, D. H. Lee, R. J. Clément, X. Yu, M. Leskes, A. J. Pell, G. Pintacuda, X.-Q. Yang, C. P. Grey and Y. S. Meng, *Chem. Mater.*, 2014, **26**, 1260–1269.

40 L. Mu, M. M. Rahman, Y. Zhang, X. Feng, X.-W. Du, D. Nordlund and F. Lin, *J. Mater. Chem. A*, , DOI:10.1039/C7TA08410B.

41 Y.-K. Sun, S.-T. Myung, M.-H. Kim, J. Prakash and K. Amine, *J. Am. Chem. Soc.*, 2005, **127**, 13411–13418.

42 Y. Tsuchiya, K. Takanashi, T. Nishinobo, A. Hokura, M. Yonemura, T. Matsukawa, T. Ishigaki, K. Yamanaka, T. Ohta and N. Yabuuchi, *Chem. Mater.*, 2016, **28**, 7006–7016.

43 L. Mu, S. Xu, Y. Li, Y.-S. Hu, H. Li, L. Chen and X. Huang, *Adv. Mater.*, 2015, **27**, 6928–6933.

44 Y. Liu, J. C. Andrews, J. Wang, F. Meirer, P. Zhu, Z. Wu and P. Pianetta, *Opt. Express*, 2011, **19**, 540.

45 Y. Liu, F. Meirer, J. Wang, G. Requena, P. Williams, J. Nelson, A. Mehta, J. C. Andrews

and P. Pianetta, *Anal. Bioanal. Chem.*, 2012, **404**, 1297–301.

46 T. L. Kao, C. Y. Shi, J. Wang, W. L. Mao, Y. Liu and W. Yang, *Microsc. Res. Tech.*, 2013, **76**, 1112–1117.

47 Y. Liu, F. Meirer, P. A. Williams, J. Wang, J. C. Andrews and P. Pianetta, *J. Synchrotron Radiat.*, 2012, **19**, 281–287.

48 P. Giannozzi, S. Baroni, N. Bonini, M. Calandra, R. Car, C. Cavazzoni, D. Ceresoli, G. L. Chiarotti, M. Cococcioni, I. Dabo, A. Dal Corso, S. de Gironcoli, S. Fabris, G. Fratesi, R. Gebauer, U. Gerstmann, C. Gougoussis, A. Kokalj, M. Lazzeri, L. Martin-Samos, N. Marzari, F. Mauri, R. Mazzarello, S. Paolini, A. Pasquarello, L. Paulatto, C. Sbraccia, S. Scandolo, G. Sclauzero, A. P. Seitsonen, A. Smogunov, P. Umari and R. M. Wentzcovitch, *J. Phys. Condens. Matter*, 2009, **21**, 395502.

49 J. P. Perdew, K. Burke and M. Ernzerhof, *Phys. Rev. Lett.*, 1996, **77**, 3865–3868.

50 S. L. Dudarev, G. A. Botton, S. Y. Savrasov, C. J. Humphreys and A. P. Sutton, *Phys. Rev. B*, 1998, **57**, 1505–1509.

51 K. F. Garrity, J. W. Bennett, K. M. Rabe and D. Vanderbilt, *Comput. Mater. Sci.*, 2014, **81**, 446–452.

52 G. L. W. Hart, L. J. Nelson and R. W. Forcade, *Comput. Mater. Sci.*, 2012, **59**, 101–107.

53 G. L. W. Hart and R. W. Forcade, *Phys. Rev. B*, 2009, **80**, 14120.

54 G. Henkelman, A. Arnaldsson and H. Jónsson, *Comput. Mater. Sci.*, 2006, **36**, 354–360.

55 Z.-Y. Li, J. Zhang, R. Gao, H. Zhang, L. Zheng, Z. Hu and X. Liu, *J. Phys. Chem. C*, 2016, **120**, 9007–9016.

56 L. G. Chagas, D. Buchholz, C. Vaalma, L. Wu and S. Passerini, *J. Mater. Chem. A*, 2014, **2**, 20263–20270.

57 F. Lin, D. Nordlund, I. M. Markus, T.-C. Weng, H. L. Xin and M. M. Doeff, *Energy Environ. Sci.*, 2014, **7**, 3077–3085.

58 L. Mu, M. M. Rahman, Y. Zhang, X. Feng, X.-W. Du, D. Nordlund and F. Lin, 2017,

submitted.

59 J. Li, R. Doig, J. Camardese, K. Plucknett and J. R. Dahn, *Chem. Mater.*, 2015, **27**, 7765–7773.

60 E. Talaie, S. Y. Kim, N. Chen and L. F. Nazar, *Chem. Mater.*, 2017, **29**, 6684–6697.

61 S.-M. Oh, P. Oh, S.-O. Kim and A. Manthiram, *J. Electrochem. Soc.*, 2017, **164**, A321–A326.

62 J. Wang, X. He, D. Zhou, F. Schappacher, X. Zhang, H. Liu, M. C. Stan, X. Cao, R. Kloepsch, M. S. Sofy, G. Schumacher and J. Li, *J. Mater. Chem. A*, 2016, **4**, 3431–3437.

63 L. Liu, X. Li, S.-H. Bo, Y. Wang, H. Chen, N. Twu, D. Wu and G. Ceder, *Adv. Energy Mater.*, 2015, **5**, 1500944.

64 S. Komaba, N. Yabuuchi, T. Nakayama, A. Ogata, T. Ishikawa and I. Nakai, *Inorg. Chem.*, 2012, **51**, 6211–6220.

65 W. Ren, Z. Zhu, Q. An and L. Mai, *Small*, 2017, **13**, 1604181.

66 J.-Y. Hwang, S.-M. Oh, S.-T. Myung, K. Y. Chung, I. Belharouak and Y.-K. Sun, *Nat. Commun.*, 2015, **6**, 6865.

67 X. Zhang, C. Fan and S. Han, *J. Mater. Sci.*, 2017, **52**, 10418–10430.

68 W.-S. Yoon, O. Haas, S. Muhammad, H. Kim, W. Lee, D. Kim, D. A. Fischer, C. Jaye, X.-Q. Yang, M. Balasubramanian and K.-W. Nam, *Sci. Rep.*, 2015, **4**, 6827.

69 K.-W. Nam, S.-M. Bak, E. Hu, X. Yu, Y. Zhou, X. Wang, L. Wu, Y. Zhu, K.-Y. Chung and X.-Q. Yang, *Adv. Funct. Mater.*, 2013, **23**, 1047–1063.

70 R. Sarangi, N. Aboelella, K. Fujisawa, W. B. Tolman, B. Hedman, K. O. Hodgson and E. I. Solomon, *J. Am. Chem. Soc.*, 2006, **128**, 8286–96.

71 X. Liu, J. Liu, R. Qiao, Y. Yu, H. Li, L. Suo, Y. Hu, Y.-D. Chuang, G. Shu, F. Chou, T.-C. Weng, D. Nordlund, D. Sokaras, Y. J. Wang, H. Lin, B. Barbiellini, A. Bansil, X. Song, Z. Liu, S. Yan, G. Liu, S. Qiao, T. J. Richardson, D. Prendergast, Z. Hussain, F. M. F. de Groot and W. Yang, *J. Am. Chem. Soc.*, 2012, **134**, 13708–13715.

72 T. Yi, W. Chen, L. Cheng, R. D. Bayliss, F. Lin, M. R. Plews, D. Nordlund, M. M. Doeff, K. A. Persson and J. Cabana, *Chem. Mater.*, 2017, **29**, 1561–1568.

73 F. Yang, Y. Liu, S. K. Martha, Z. Wu, J. C. Andrews, G. E. Ice, P. Pianetta and J. Nanda, *Nano Lett.*, 2014, **14**, 4334–4341.

Acknowledgement

The work was supported by Virginia Tech Department of Chemistry startup funds. The Stanford Synchrotron Radiation Lightsource, a Directorate of SLAC National Accelerator Laboratory and an Office of Science User Facility is operated for the US Department of Energy Office of Science by Stanford University. Use of the Stanford Synchrotron Radiation Lightsource, SLAC National Accelerator Laboratory, is supported by the US Department of Energy, Office of Science, Office of Basic Energy Sciences under Contract No.DE-AC02-76SF00515. M.M.R, Y.X., Y.L. and F.L. thank D. Van Campen and Dave Day for valuable discussions and their engineering support for experiments at beamline 6-2C of SSRL. The authors acknowledge Special Program for EApplied Research on Super Computation of the NSFC-Guangdong Joint Fund (the second phase) under Grant No. U1501501. The authors also acknowledge Stephen McCartney for his assistance in SEM at the Nanoscale Characterization and Fabrication Laboratory at Virginia Tech. The authors would further like to acknowledge Dr. Tom Staley for his technical assistance with XRD in Material Science and Engineering at Virginia Tech. This research used resources of the Advanced Photon Source, an Office of Science User Facility operated for the U.S. Department of Energy (DOE) Office of Science by Argonne National Laboratory, and was supported by the U.S. DOE under Contract No. DE-AC02-06CH11357, and the Canadian Light Source and its funding partners.

Author contribution

F.L. conceived and directed the project. M.M.R. performed synthesis, performance testing and characterization. Q.S. assisted the synthesis. Y.X. and Y.L. collected and analyzed the TXM data. L.M. assisted in the TXM data acquisition. S.X. assisted in the TXM data analysis. M.M.R.,

L.M., R.K., Q.L., X.X., C.S., D.S. and D.N. performed X-ray spectroscopy and diffraction. H.C. and J.C.Z performed the DFT calculation. M.M.R. and F.L. analyzed the data and wrote the manuscript with assistance from all the coauthors.